Journal of Controlled Release 172 (2013) 274–280

Contents lists available at ScienceDirect

Journal of Controlled Release

journal homepage: www.elsevier.com/locate/jconrel

Drug delivery to the brain by focused ultrasound induced blood–brain barrier disruption: Quantitative evaluation of enhanced permeability of cerebral vasculature using two-photon microscopy

Tam Nhan [a,b,*], Alison Burgess [a], Eunice E. Cho [a], Bojana Stefanovic [a,b], Lothar Lilge [b,c], Kullervo Hynynen [a,b]

[a] Physical Sciences, Sunnybrook Research Institute, Toronto, ON, Canada
[b] Medical Biophysics, University of Toronto, Toronto, ON, Canada
[c] Ontario Cancer Institute, Princess Margaret Hospital, Toronto, ON, Canada

ARTICLE INFO

Article history:
Received 30 May 2013
Accepted 24 August 2013
Available online 2 September 2013

Keywords:
Blood–brain barrier
Focused ultrasound
Drug delivery
Permeability
Two-photon fluorescence microscopy

ABSTRACT

Reversible and localized blood–brain barrier disruption (BBBD) using focused ultrasound (FUS) in combination with intravascularly administered microbubbles (MBs) has been established as a non-invasive method for drug delivery to the brain. Using two-photon fluorescence microscopy (2PFM), we imaged the cerebral vasculature during BBBD and observed the extravasation of fluorescent dye in real-time *in vivo*. We measured the enhanced permeability upon BBBD for both 10 kDa and 70 kDa dextran conjugated Texas Red (TR) at the acoustic pressure range of 0.2–0.8 MPa and found that permeability constants of TR10kDa and TR70kDa vary from 0.0006 to 0.0359 min^{-1} and from 0.0003 to 0.0231 min^{-1}, respectively. For both substances, a linear regression was applied on the permeability constant against the acoustic pressure and the slope from best-fit was found to be 0.039 ± 0.005 min^{-1}/MPa and 0.018 ± 0.005 min^{-1}/MPa, respectively. In addition, the pressure threshold for successfully induced BBBD was confirmed to be 0.4–0.6 MPa. Finally, we identified two types of leakage kinetics (fast and slow) that exhibit distinct permeability constants and temporal disruption onsets, as well as demonstrated their correlations with the applied acoustic pressure and vessel diameter. Direct assessment of vascular permeability and insights on its dependency on acoustic pressure, vessel size and leakage kinetics are important for treatment strategies of BBBD-based drug delivery.

1. Introduction

Intensive efforts in drug development have led to the formation of numerous therapeutics with the potential to treat central nervous system (CNS) diseases and disorders including chemotherapeutic agents for the treatment of brain tumors and metastases [1] as well as chemokines, growth factors, and viral vectors for the treatment of neurodegenerative diseases [2–4]. However, the blood–brain barrier (BBB) prevents more than 98% of the existing pharmaceutical agents from entering the brain tissue [5,6] thereby limiting the application of these potential therapeutics in the CNS. Research efforts are underway to develop clinically viable methods to deliver therapeutic drugs into the CNS safely and effectively such as drug modification to promote carrier-mediated or receptor-mediated transport [7,8] as well as intra-carotid infusion of hyper-osmotic solutions to cause the widening of tight junctions [9,10].

Recently, focused ultrasound (FUS) in combination with microbubble (MB) contrast agent has been used as a non-invasive method to induce BBB disruption (BBBD) for spatially targeted drug delivery to the brain [11]. Inside the blood vessel, under the influence of the FUS beam, MBs expand and contract via inertial cavitation or stable cavitation processes [12–15]. These physical activities exert mechanical forces (i.e. shear and circumferential stresses) onto proximal capillary walls [16] leading to increased paracellular transport through widened tight junctions [17], and/or increased transcellular transport through activation of carrier proteins or pore formation [18–21]. In general, localization of the BBB opening is dictated by the focal volume of the FUS beam and the presence of MBs which reduce the ultrasound energy required for BBBD so that thermal effects and tissue damage can be minimized. Using FUS, effective drug concentrations can be achieved locally while their accumulation elsewhere in the brain and body can be limited, hence decreasing non-specific effects.

Guidance and evaluation of FUS-induced BBBD has been primarily performed by magnetic resonance imaging (MRI). Typically, T1-weighted MR images are acquired to confirm successful delivery of Gadolinium based MR contrast agents across the BBB [11,22,23], whereas T2-weighted MR images serve to verify the absence of edema and tissue damage [24,25]. In addition, quantitative measurement of the permeability of the BBB in the targeted region (e.g. hippocampus or striatum) can be done via dynamic contrast enhanced MRI (DCE-MRI) [26–29]. However, spatial resolution (e.g. lateral: 86 × 86 μm^2;

* Corresponding author at: Physical Sciences, Sunnybrook Research Institute, C713-2075 Bayview Ave, Toronto, ON M4N 3M5, Canada. Tel.: +1 289 200 7245; fax: +1 416 480 5714.
E-mail address: tnhan@sri.utoronto.ca (T. Nhan).

0168-3659/$ – see front matter © 2013 Elsevier B.V. All rights reserved.
http://dx.doi.org/10.1016/j.jconrel.2013.08.029

slice thickness: 500 μm) offered by MRI limits permeability measurement to a macroscopic brain volume of 2–35 mm^3 [28,29].

To advance knowledge of the microscopic mechanisms associated with FUS-induced BBBD, we proposed using two-photon fluorescence microscopy (2PFM) which allows sufficient temporal and spatial resolution to track transient changes in BBB permeability at a microvascular level. Beyond volumetric average as achieved in DCE-MRI, we hope to resolve the gradient of drug concentration to differentiate therapeutic range from toxicity level using 2PFM. Proof-of-concept in monitoring BBBD using 2PFM had been demonstrated by Raymond et al. [30,31]. In that study, the authors injected fluorescent dyes (e.g. Texas Red, Oregon Green) for the visualization of the microvasculature and transmitted ultrasound from the ventral surface of the brain to induce BBBD. With this setup, the authors identified two leakage responses: micro-disruption and slow disruption. The former is characterized by a focal eruption of dye from a single point on the vessel wall, whereas the latter is characterized by a slower and more spatially-extended leakage. Using a dorsal approach for application of FUS, our group was able to reliably induce BBBD with a better-controlled in situ applied acoustic pressure [32,33]. These studies characterized the microscopic leakage patterns qualitatively but did not attempt to quantify the rate of agent delivery.

Here, we demonstrate a quantitative approach to analyze the 2PFM images post-BBBD. By extracting and correlating intravascular and extravascular signals from the time-lapse 2PFM images, a permeability constant of the cerebral vasculature network within the imaging field of view (FOV) can be determined. Measured vascular permeability is then correlated with the applied acoustic pressure, disruption onset and vessel diameter to shed light on the potential mechanisms which control BBBD. These insights are crucial for guiding future treatments utilizing BBBD-based drug delivery to the brain.

2. Material and methods

2.1. Animal preparation

Male Wistar rats of 150–250 g weight range were used in this study (n = 40). All the procedures were approved by the institutional Animal Care and Use Committee and were in accordance with the guideline by Canadian Council on Animal Care. The animals were initially anesthetized with 5% isoflurane, which was later reduced to 2%. The animals were positioned in a stereotactic frame and the head was immobilized using ear and bite bars (Fig. 1A). The skull and dura were removed to create a 5 mm diameter cranial window over the right hemisphere, approximately 3 mm lateral from the midline and 3 mm posterior to the bregma. The cranial window was filled with 1% agarose and the transducer attached to a coverslip of 12 mm diameter and 150 μm thickness was secured on top of the cranial window by cyanoacrylate glue (Fig. 1A). The tail vein was cannulated with a 23-G needle and 70 mm polyethylene tubing for the injection of fluorescent dye and MB contrast agents. Once the surgery was completed, the stereotactic stage was transferred to the microscope for BBBD induction and 2PFM imaging.

2.2. FUS parameters for BBBD

The experimental timeline is shown in Fig. 1B. Prior to sonication, Definity MBs (Lantheus Medical Imaging, Billerica, MA, USA) of 1.1–3.3 μm mean diameter were diluted with saline (1:10 v/v) and injected through the tail vein at a final concentration of 0.02 ml/kg. A PZT-4 cylindrical transducer (diameter = 10 mm, thickness = 1.5 mm, height = 1.1 mm) was used for sonication. A complete characterization study of the transducer design, which facilitates dorsal application of FUS and simultaneous 2PFM imaging, has been described previously in [33]. Briefly, the transducer was operated in the thickness mode at a frequency of 1.2 MHz to produce a circularly uniform

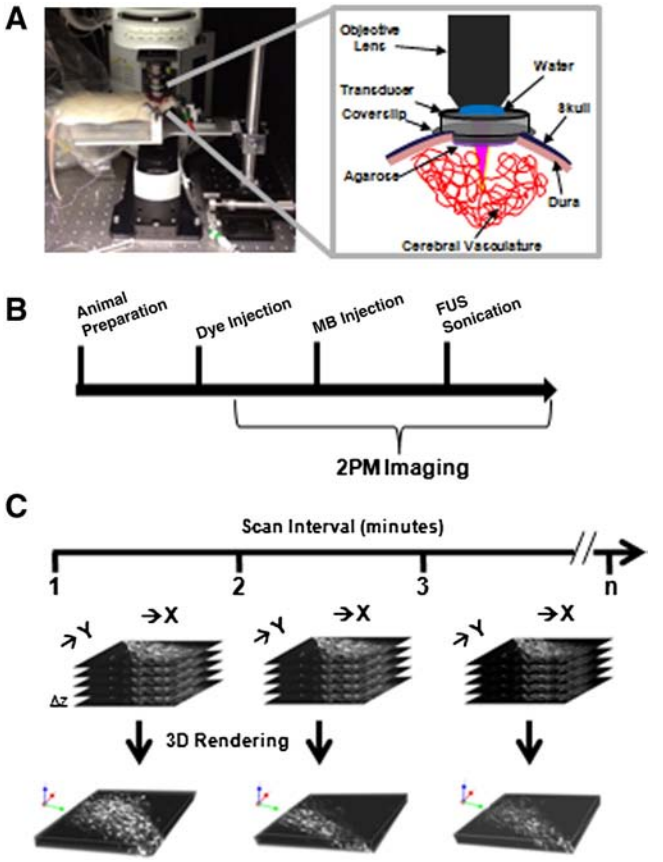

Fig. 1. *In vivo* BBBD induced by FUS and monitored by 2PFM imaging. A) Schematic of the experimental setup used to induce BBBD in rats via MBs & FUS. Ring configuration of the transducer also facilitates optical transparency for 2PFM imaging. B) Experimental timeline. C) 4D XYZT acquisition of 2PFM imaging.

focal spot that coincides with the microscope's lateral imaging FOV (512 × 512 μm^2). The ultrasound depth of field generated by the transducer is shallow (1 mm immediately beneath the coverslip), ensuring that it overlapped with the light depth penetration of the 2PFM. The transducer was driven by a function generator (Agilent, Palo Alto, CA, USA) and a 53 dB RF power amplifier (NP Technologies Inc., Newbury Park, CA, USA) with typical BBBD sonication parameters (10 ms pulse duration, 1 Hz pulse repetition frequency, 120 s total sonication duration). The applied forward and reflected RF-power during sonication was recorded using an in-house constructed power meter.

2.3. 2PFM imaging

To visualize the cerebral vasculature, 10 kDa or 70 kDa dextran-conjugated Texas Red (Invitrogen, Burlington, ON, Canada) was injected through the tail vein. The two molecular weights (MWs) were chosen to represent equivalent therapeutic substances with sizes ranging from small proteins and siRNAs up to albumin-bound drugs that can be delivered across the BBB. The animal was positioned below the microscope stage (FV1000MPE, Olympus, Tokyo, Japan) and the cranial window was aligned underneath a water-immersion objective (Olympus XLPLN, Tokyo, Japan) with 25× magnification power, 1.05 numerical aperture and 2 mm working distance. Two-photon excitation of Texas Red fluorescent dye was achieved with a mode-lock Ti:Sapphire laser unit (Mai-Tai, Spectra-Physics, Mountain View, CA, USA) emitting at 810 nm wavelength, 100 fs pulse width and 80 MHz repetition rate. Scanning was performed in an XYZT order (Fig. 1C), in which lateral images of 512 × 512 pixels (0.99 μm resolution, 8 μs/pixel) were captured below the cortical surface up to 300 μm depth (i.e. cortical layers I and II) in a stacking mode at 10 μm increments. This stacking distance

allows imaging of pial vessels as well as penetrating vessels and capillaries. As depicted in Fig. 1B, 2PFM imaging was continuous over the course of the experiment; from the injection of MBs, through the 120 s sonication, and following leakage of the fluorescent dye upon BBBD. Typically, each data set consists of 40–50 stacks with the acquisition time of 15 to 30 s per stack.

2.4. Analysis of 2PFM data

4D XYZT microscopic data of a superficial cortical tissue volume was visualized in MATLAB (The MathWorks, Natick, MA, USA) as a maximum intensity projection map along z direction (Fig. 2A). To separate the intravascular and extravascular compartments, automatic vessel segmentation was performed on each individual Z-slice at the initial time point (when BBB was impermeable to either dextran). Once the intravascular regions of interest (ROIs) were masked based on the segmented vessels, extravascular ROIs were identified by subtracting the intravascular ROIs from the imaging FOV. Fluorescent intensity associated with each compartment, $I_i(t)$ and $I_e(t)$, was then calculated by averaging over all pixels within the compartment ROIs over the entire depth (Fig. 2B).

To measure permeability from fluorescent intensity change in the intravascular and extravascular spaces, we applied the formulation developed by Dreher et al. [34]. In their model, the rate of solute transport across a blood vessel wall is given by the Kedem–Katchalsky equation to account for both convection and diffusion processes [34–36]. However, due to its unknown direction and magnitude, the convective term was ignored and its influence was lumped into the latter term [37]. Given the linearity between the dye concentration and the fluorescent signal intensity in the plasma and the extravascular space, an apparent permeability $\alpha(t)$ measuring exchange capacity between the two compartments can be determined via the following equation:

$$\alpha(t) = \frac{dI_e/dt}{\frac{I_i(t)}{1-HCT} - \frac{I_e(t)}{V_e/V_i}}$$

where V_e/V_i is the volume fraction between extravascular and intravascular compartments, which was simply obtained from the vessel segmentation. Similar to DCE-MRI studies by Park et al. [27] and Vlachos et al. [28,29], HCT of 45% was assigned to account for the average hematocrit level of all blood vessels within the imaging FOV [38,39]. Apparent permeability α_{app} for each studied subject is the average value of $\alpha(t)$ from 3 to 30 min, corresponding to the peaked duration of BBBD (Fig. 2C).

2.5. Statistical analysis

At each acoustic pressure, the apparent permeability α_{app} of TR10kDa and TR70kDa, as well as the volume fraction V_i/V_e, were reported as mean (± standard deviation) over 5 animal subjects. For 40 cases of permeability measurements, comparison among 4 pressure groups and 2 molecular

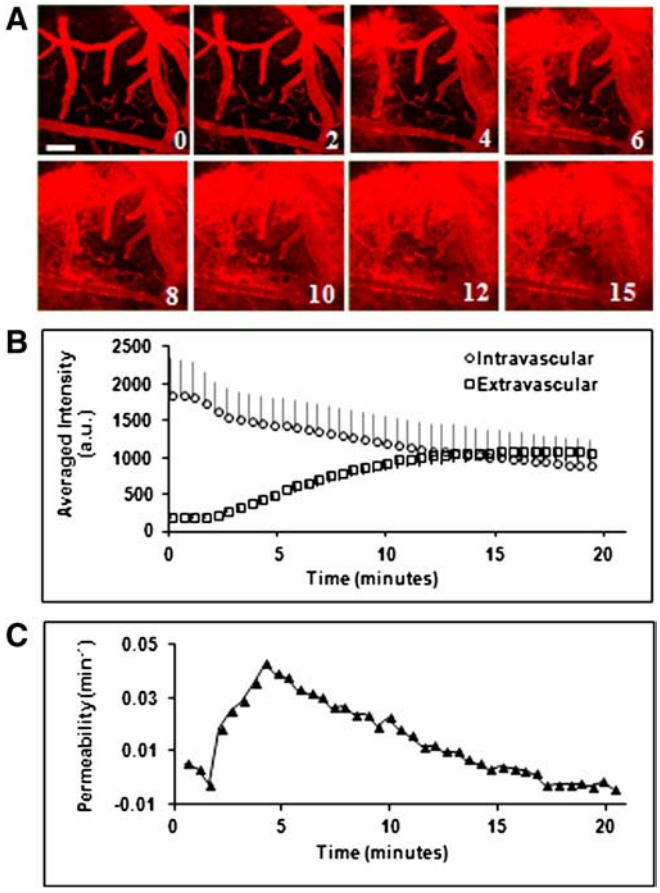

Fig. 2. Data analysis of 2PFM data capturing fluorescent dye leakage upon BBBD. A) Depth projection images illustrate the transient BBBD induced by MBs & FUS at 0.6 MPa (scale bar: 100 μm). Sonication and MB injection occurred during the first 2 min while the vessels remained impermeable to dextran conjugated Texas Red TR10kDa. As soon as sonication ceased, disruption started at multiple vessels within the imaging FOV and extravascular signal increases over time. B) Quantitative measurement of averaged fluorescent signal intensities associated with intravascular and extravascular compartments over time. C) Permeability was evaluated accordingly.

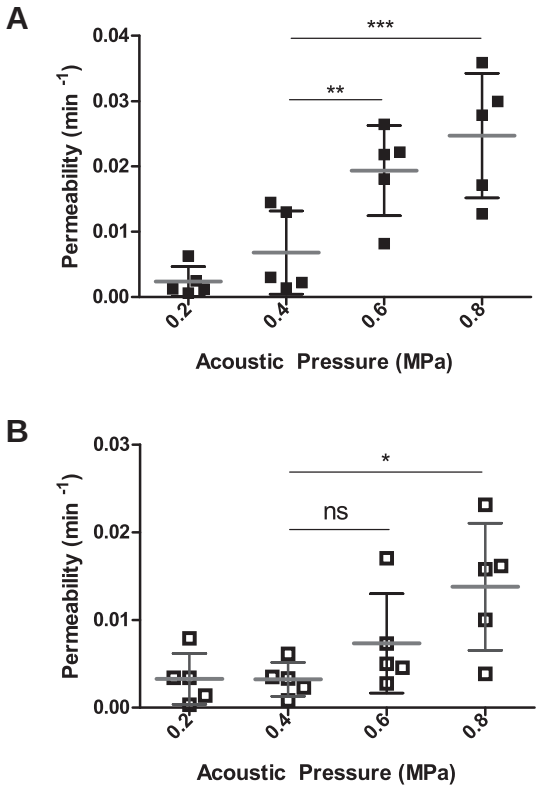

Fig. 3. Effect of acoustic pressure on permeability dextran conjugated Texas Red across the BBB. A) Measured for all 20 cases of TR10kDa delivered across the BBB (n = 5 per pressure). Two-way ANOVA in combination with Bonferroni post-tests confirms statistical significance in permeability induced at low pressure of 0.4 MPa with respect to the higher acoustic pressure of 0.6 MPa and 0.8 MPa. B) Measured permeabilities for all 20 cases of TR70kDa delivered across the BBB (n = 5 per pressure). Two-way ANOVA in combination with Bonferroni post-tests suggests that there is no statistical significance in permeabilities between the 0.4 MPa and 0.6 MPa, whereas statistical significance was found for permeabilities induced at 0.4 MPa and 0.8 MPa.

weights (MW = 10 kDa and 70 kDa) was performed using two-way ANOVA followed by Bonferroni post-tests in GraphPad Prism (GraphPad Software Inc., CA, USA). Correlation between the acoustic pressure and BBBD temporal onset was evaluated by one-way ANOVA followed by Bonferroni's Multiple Comparison Test. Distinction between vessel size distribution and leakage type (fast vs. slow kinetics) was assessed using two-tailed unpaired Student's t test. For all of these analyses, $p < 0.05$ was considered statistically significant.

3. Results

3.1. Effect of acoustic pressure on enhanced BBB permeability

For TR10kDa and TR70kDa, we analyzed 5 data sets per pressure and the evaluated permeability values are presented in Fig. 3A and B, respectively. Both scattering plots reveal an increasing trend for the permeability at higher pressure. To quantitatively explore the relationship of permeability and acoustic pressure, linear regression was applied for each MW. Best-fit values of slope for TR10kDa and TR70kDa were found to be 0.039 ± 0.005 min^{-1}/MPa and 0.018 ± 0.005 min^{-1}/MPa, respectively. Best-fit values of X-intercept for TR10kDa and TR70kDa were found to be 0.16 MPa and 0.11 MPa, respectively. In addition, two-way ANOVA in combination with Bonferroni post-tests confirmed statistical significance in permeability of TR10kDa induced at low acoustic pressure of 0.4 MPa with respect to higher acoustic pressure of 0.6 MPa and 0.8 MPa. For TR70kDa, no significant difference of permeability between 0.4 MPa and 0.6 MPa was found, whereas statistical significance was observed for resulting permeabilities at 0.4 MPa and 0.8 MPa.

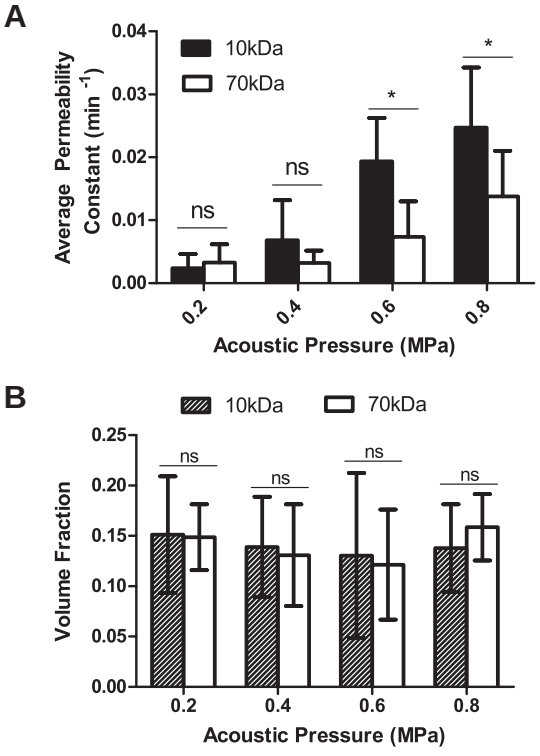

Fig. 4. Effect of substance size on enhanced BBB permeability. A) At each pressure, average permeability constant (n = 5) was compared between TR10kDa and TR70kDa. Two-way ANOVA in combination with Bonferroni post-tests was performed as multiple comparisons. The p values at high pressure (0.6 MPa and 0.8 MPa) are statistically significant, elucidating different levels of permeability enhancement between two MWs. B) At each pressure, average volume fraction (n = 5) was compared between TR10kDa and TR70kDa. Two-way ANOVA in combination with Bonferroni post-tests was performed as multiple comparisons and confirmed that there was no statistical significant between each MW pair across all 4 acoustic pressures.

3.2. Effect of substance size on enhanced BBB permeability

To determine the impact of substance size (or MW) on BBB permeability, average values of two MWs at similar acoustic pressure are plotted side by side as shown in Fig. 4A. Two-way ANOVA followed by Bonferroni post-tests confirmed that the difference in enhanced permeability between the two MWs at 0.2 MPa and 0.4 MPa was not significant. However, at high pressure, a significantly greater permeability of TR10kDa compared to TR70kDa was demonstrated (e.g. $p < 0.05$ at 0.6 MPa and 0.8 MPa), which is consistent with the expected inverse relationship between molecular size and its permeation across the BBB. To confirm that these permeability measurements were not confounded by differences in cerebral vasculature volume, two-way ANOVA followed by Bonferroni post-tests was performed on the volume fraction V_i/V_e between TR10kDa and TR70kDa at 4 acoustic pressure levels (n = 5 per group) and found no statistically significant differences for all 4 pairs.

3.3. Temporal onset of BBBD is correlated with permeability and appears to be controlled by acoustic pressure

To investigate the kinetics of BBBD, temporal onset (i.e. time point when leakage was initiated) was recorded for all 40 data sets and plotted against the permeability. As evident in Fig. 5A, an inverse relationship between these two entities was observed. 10 min was chosen as the temporal benchmark to separate fast leakage from slow leakage as this duration is the averaged time required for receptor-mediated transcytosis [39,40]. Fast leakage exhibits short BBBD onset and substantially higher permeability constants, whereas slow leakage presents delayed BBBD onset and very small permeability.

To examine the connection between BBBD onset and the applied acoustic pressure, averaged temporal onset was plotted at each pressure (n = 10 per pressure), as shown in Fig. 5B. Due to its gradual increase in

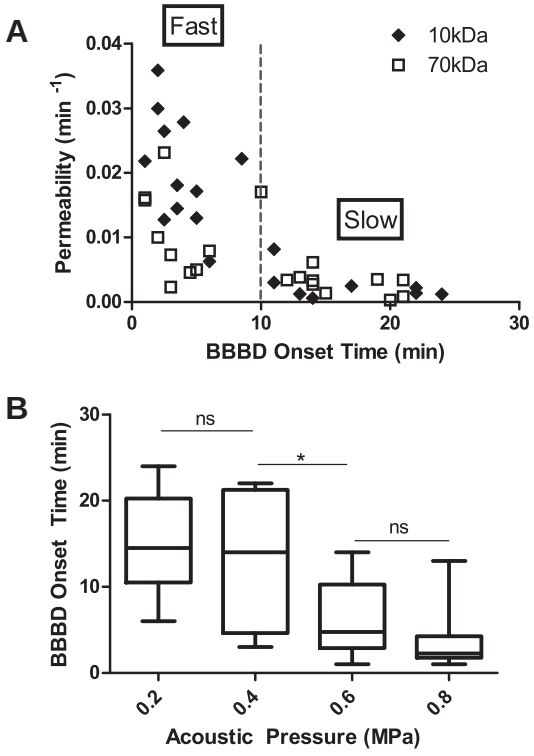

Fig. 5. BBBD onset in relation to permeability and acoustic pressure. A) Inverse relationship between BBBD onset and permeability. B) Inverse relationship between BBBD onset and acoustic pressure. One-way ANOVA followed by Bonferroni's Multiple Comparison Test confirms a statistical significance in BBBD onset between 0.4 MPa and 0.6 MPa.

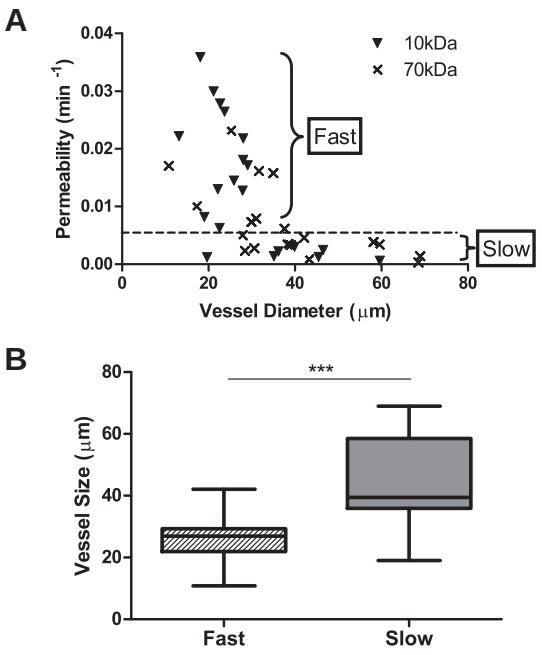

Fig. 6. Effect of vessel diameter on enhanced BBB permeability. A) Vessel size distribution in correlation with permeability constant: large vessels (20–70 μm) are prone to slow leakage kinetics and low permeability; whereas smaller vessels (10–30 μm) are subjected to fast leakage kinetics and high permeability. B) Statistical analysis (two-tailed *t* test) indicates significant difference ($p < 0.0001$) in vessel size responsible for fast and slow leakage types.

leakage, it is difficult to define BBBD onset time based on the extravascular signal curve (e.g. Fig. 2B). Therefore, we used the peak time of the permeability curve (e.g. Fig. 2C) as the benchmark for BBBD onset time. In doing so, we further noted that the peak time of approximately 4–5 min agrees with visible leakage evidence of Texas Red extravasating out of initially intact vasculature as shown in Fig. 2A.

Overall, higher pressure appears to yield prompt onset. One-way ANOVA followed by Bonferroni's Multiple Comparison Test reported no statistical significance between 0.2–0.4 MPa and 0.6–0.8 MPa, whereas significant difference between average BBBD onset at 0.4 MPa (13.5 ± 7.6 min) and at 0.6 MPa (6.3 ± 4.3 min) was noted. This strongly suggests that different leakage kinetics (slow or fast) can be controlled via the applied acoustic pressure.

3.4. Effect of vessel diameter on enhanced BBB permeability

We further looked into the effect of vessel diameter on the enhancement of BBB permeability by measuring the average diameter of vessels undergoing disruption within the imaging FOV and plotting the value against the corresponding permeability constant as illustrated in Fig. 6A. Overall, permeability appears to be inversely related to vessel diameter. By applying the predefined criteria (10 min benchmark of BBBD onset and negligible permeability constant), data points associated with fast and slow leakage are separated by the dotted line in Fig. 6A. Here, we noted that fast leakage is prevalent in small vessels (10–30 μm diameter), whereas slow leakage occurs more commonly in larger vessels (30–70 μm diameter). As revealed in Fig. 6B, *p* value from two-tailed unpaired Student's *t* test confirms the statistical significance in vessel size distribution with respect to leakage type.

4. Discussion

Past investigations into the kinetics of BBBD permeability had been carried out using DCE-MRI. For instance, Vlachos et al. demonstrated the reconstructed permeability map of the murine hippocampus superimposed onto coronal and transverse T1 images of the brain [28,29]. The same group also confirmed the dependence of permeability on acoustic pressures and microbubble sizes. Park et al. further compared the permeability enhancement of double sonication to single sonication. These analyses supported the use of DCE-MRI as an *in vivo* tool for quantifying the efficacy of FUS induced BBB opening. However, detecting disruption and measuring permeability at vascular level is of fundamental importance for resolving concentration gradients of the delivered drugs, from which therapeutic range and excessive toxicity range can both be identified. Furthermore, permeability provides estimation of drug concentration in the interstitial space. To perform these analyses, 2PFM is required.

Our study builds on the initial work of Raymond et al. who demonstrated the use of 2PFM for a comprehensive investigation of BBBD [31]. Our previously published study has advanced this field by introducing dorsally applied FUS which enhances the robustness of BBBD at a reliable in situ pressure [32,33]. In the present work, we presented a quantitative analysis technique which allows for characterization of permeability from 2PFM time-lapsed images. High spatial resolution from 2PFM imaging enabled discerning investigation into vessel diameter and the temporal onset of BBBD in correlation with applied acoustic pressure and resulting disruption kinetics.

Permeability constants had been previously reported for 1 kDa Gadolinium diethylenetriamine penta-acetic acid (Gd-DTPA) via DCE-MRI measurement as $1.1e-2\ min^{-1}$ and $3.9e-2\ min^{-1}$ when BBBD was achieved at frequency of 1.5 MHz and acoustic pressure of 0.45 MPa and 0.6 MPa, respectively [29]. At comparable FUS parameters, these values are two-fold and five-fold higher than 2PFM monitored BBB permeability enhancement of TR10kDa and TR70kDa, respectively. Although differences in permeability are expected due to its ten-fold smaller size, the distinctions between the two imaging modalities should be noted. In 2PFM, a small cortical tissue volume ($512 \times 512 \times 100\ \mu m^3$) is directly measured and vessels of narrow size distribution undergoing BBBD are readily detected. In contrast, value reported from DCE-MRI is corresponding to a much larger brain tissue volume (2–35 mm^3) [27–29] that contains only a fraction of vessels at broader size distribution being disrupted while the rest of vascular tree remain intact. Nevertheless, these data fit the overall expected trend of an inverse correlation between MW and permeability constant and eliminate the need to conduct further 2PFM on small MW compounds. Furthermore, we speculate that the permeability of large molecule therapeutics would follow the same trend as seen here and thus exhibit lower permeability than the 70 kDa compound. However, one limitation of this study is that we cannot predict how drugs with charges or other modifications will extravasate upon BBBD. Similarly, stem cells and immune cells have been shown to cross the BBB upon the application of FUS + MBs [41,42]. Due to the ability of the cells to interact with the BBB, understanding the kinetics may require further analysis.

From this study, we also noted that the permeability constant is linearly related to the applied acoustic pressure, as well as inversely related to the onset of BBBD. This observation can be explained by higher acoustic pressure resulting in greater oscillatory amplitude of MBs that induce vascular effects, and/or inertial cavitation, which triggers the collapse of MBs [12]. These MB activities could readily prompt the opening of BBB. We also observed that transition from low to high permeability (Fig. 3), as well as from long to short BBBD onset (Fig. 5B) takes place at the pressure range of 0.4–0.6 MPa. This transitional pressure agrees well with the expected pressure of 0.5 MPa when considering the operating frequency of 1.2 MHz used in our 2PFM-guided experiment and the mechanical index for BBBD threshold of 0.46 [43].

By classifying the leakage types into fast and slow kinetics based on BBBD onset (Fig. 5A), we found 20 out of 22 data points in the first group exhibiting high permeability (from $0.005\ min^{-1}$ up to $0.036\ min^{-1}$). On the other hand, in the latter group, 16 out of 18 data points possess permeability constants below $0.005\ min^{-1}$. Mechanistically, we

speculate that the fast leakage is caused by the opening tight junctions, leading to fluorescent dye leakage out of the blood vessel. In some cases, $I_e(t)$ curve exhibits saturation after the initial ramp-up (15–20 min post-sonication), indicating quick repair and closure of the BBB of a few vessels in the imaging FOV. One study suggested that a possible mechanism for quick repair involves the recruitment of astrocytes and microglia to the disruption site [44]. Although opening of tight junctions might be responsible for the typical focal pattern of disruption, another possible mechanism of fast leakage is cellular sonoporation [19]. This might explain why some fast leakage occurred extensively along a segment of blood vessel rather than from a single focal point. Notably for this mechanism, the pores also reseal quickly (4–10 s) [45]. In contrast, we predict that slow leakage is facilitated by transcytosis, which is limited under normal condition of the BBB. However, FUS-induced oscillation of MBs may activate endothelial cell receptors to promote transcellular transport of molecules from the lumen to interstitial space [18,21,46]. It was previously suggested that transcytosis of low-density lipoproteins across the endothelial cells lining the vessel wall takes at least 15 min [39]. This lag may account for the slow onset of leakage observed in our 2PFM experiments.

As reflected in the permeability constant, the extent of BBB opening is inversely related to the vessel diameter (Fig. 6A). In a simulation study, Hosseinkhah and Hynynen had shown similar dependency of shear stress on the ratio between vessel and initial bubble radii (i.e., largest shear stresses were obtained at lowest r_v/r_0 values) [16]. Based on this data, we speculate that when MBs with a narrow size distribution are administered, smaller vessels will experience higher shear stress and be more prone to BBB opening. This conjecture also describes the observed link between vessel size and leakage type (shown in Fig. 6B), where smaller vessels are more inclined to undergo fast leakage due to the applied shear stress, while slow leakage is predominately seen in larger vessels under trigger by minor perturbations and activation of cellular receptors. Furthermore, this notion is in agreement with electron microscopy observations where higher level of active vesicular transport of blood-borne tracer molecules was found in the arterioles as compared to the capillaries [21].

Lastly, the enhanced permeability, time of BBBD onset, and leakage kinetics (fast vs. slow) are affected by the applied acoustic pressure. This suggests that it is possible to control the leakage type and tailor drug delivery for specific treatment procedures by altering the FUS parameters. For instance, the high permeability and prompt opening associated with fast leakage may benefit delivery of small MW drugs with short plasma half-lives. In contrast, slow leakage may be more suitable for delivery of large MW substances, with increased plasma half-lives that allows for extended availability for transcytocis across the BBB. In fact, by considering the difference in plasma half-lives between 10 kDa and 70 kDa agent (e.g. 10 min vs. 25 min [34]) and their averaged permeability constant associated with fast leakage (e.g. 0.0205 min^{-1} vs. 0.0110 min^{-1}, respectively (Fig. 6A)), we calculated the accumulation of each agent delivered to the extravascular compartment over 1 h. As a result, the fraction of concentration–time area under the curve (AUC) between extravascular space and plasma was estimated for 10 kDa and 70 kDa agent to be 0.61 and 0.35, respectively. Meanwhile, given a low averaged permeability constant of 0.0025 min^{-1} for both MWs (Fig. 6A), the fraction of concentration–time AUC between the two compartments was found to be relatively comparable (e.g. 0.11 for 10 kDa and 0.09 for 70 kDa). Therefore, this quantitative approximation supports the aforementioned postulations on suitable delivery approaches for therapeutic agent of different MWs (e.g. fast leakage for small MWs and slow leakage for large MWs).

Acknowledgments

The authors would like to thank Shawna Rideout-Gros and Alexandra Garces for their help with animal care; Adrienne Dorr for her guidance in using the two-photon fluorescence microscope for our *in vivo* studies; and Shirley Miao for her assistance in developing Matlab vessel segmentation algorithm. This work was supported in part by National Institutes of Health under grant # R01 EB003268 (Kullervo Hynynen), Canadian Institutes of Health Research under grant # CIHR FRN 119312 (Kullervo Hynynen) and Natural Sciences and Engineering Research Council of Canada under NSERC CGS-D3 scholarship (Tam Nhan).

References

[1] J.T. Huse, E.C. Holland, Targeting brain cancer: advances in the molecular pathology of malignant glioma and medulloblastoma, Nat. Rev. Cancer 10 (2010) 319–331.
[2] H.L. Weiner, D. Frenkel, Immunology and immunotherapy of Alzheimer's disease, Nat. Rev. Immunol. 6 (2006) 404–416.
[3] M.H. Tuszynski, Growth-factor gene therapy for neurodegenerative disorders, Lancet Rev. 1 (2002) 51–57.
[4] S.T. Lim, M. Airavaara, B.K. Harvey, Viral vectors for neurotrophic factor delivery: a gene therapy approach for neurodegenerative diseases of the CNS, Pharmacol. Res. 61 (2010) 14–26.
[5] G.W. Goldstein, A.L. Betz, The blood–brain barrier, Sci. Am. 255 (1986) 74–83.
[6] W.M. Pardridge, The blood–brain barrier: bottleneck in brain drug development, NeuroRx 2 (2005) 3–14.
[7] A.T. Nies, The role of membrane transporters in drug delivery to brain tumors, Cancer Lett. 254 (2007) 11–29.
[8] L. Juillerat-Jeanneret, The targeted delivery of cancer drugs across the blood–brain barrier: chemical modifications of drugs or drug-nanoparticles? Drug Discov. Today 13 (2008) 1099–1106.
[9] S.I. Rapoport, Advances in osmotic opening of the blood–brain barrier to enhance CNS chemotherapy, Expert. Opin. Investig. Drugs 10 (2001) 1809–1818.
[10] D.F. Kraemer, D. Fortin, E.A. Neuwelt, Chemotherapeutic dose intensification for treatment of malignant brain tumors: recent developments and future directions, Curr. Neurol. Neurosci. Rep. 2 (2002) 216–224.
[11] K. Hynynen, N. McDannold, N. Vykhodtseva, F.A. Jolesz, Noninvasive MR imaging — guided focal opening of the blood–brain barrier in rabbits, Radiology 220 (2001) 640–646.
[12] N. McDannold, N. Vykhodtseva, K. Hynynen, Targeted disruption of the blood–brain barrier with focused ultrasound: association with cavitation activity, Phys. Med. Biol. 51 (2006) 793–807.
[13] M.A. O'Reilly, K. Hynynen, Feedback-controlled focused ultrasound disruption by using an acoustic emissions-based controller, Radiology 263 (2012).
[14] M.A. O'Reilly, K. Hynynen, Ultrasound enhanced drug delivery to the brain and central nervous system, Int. J. Hyperth. 28 (2012) 386–396.
[15] A. Burgess, K. Hynynen, Noninvasive and targeted drug delivery to the brain using focused ultrasound, ACS Chem. Neurosci. 4 (2013) 519–526.
[16] N. Hosseinkhah, K. Hynynen, A three-dimensional model of an ultrasound contrast agent gas bubble and its mechanical effects on microvessels, Phys. Med. Biol. 57 (2012) 785–808.
[17] N. Sheikov, N. McDannold, S. Sharma, K. Hynynen, Effect of focused ultrasound applied with an ultrasound contrast agent on the tight junctional integrity of the brain microvascular endothelium, Ultrasound Med. Biol. 34 (2008) 1093–1104.
[18] J. Deng, Q. Huang, F. Wang, Y. Liu, Z. Wang, Z. Wang, et al., The role of caveolin-1 in blood–brain barrier disruption induced by focused ultrasound combined with microbubbles, J. Mol. Neurosci. 46 (2012) 677–687.
[19] A. van Wamel, K. Kooiman, M. Harteveld, M. Emmer, F.J. ten Cate, M. Versluis, et al., Vibrating microbubbles poking individual cells: drug transfer into cells via sonoporation, J. Control. Release 112 (2006) 149–155.
[20] B.D.M. Meijering, L.J.M. Juffermans, A. van Wamel, R.H. Henning, I.S. Zuhorn, M. Emmer, et al., Ultrasound and microbubble-targeted delivery of macromolecules is regulated by induction of endocytosis and pore formation, Circ. Res. 104 (2009) 679–687.
[21] N. Sheikov, N. McDannold, F. Jolesz, Y.-Z. Zhang, K. Tam, K. Hynynen, Brain arterioles show more active vesicular transport of blood-borne tracer molecules than capillaries and venules after focused ultrasound-evoked opening of the blood–brain barrier, Ultrasound Med. Biol. 32 (2006) 1399–1409.
[22] N. McDannold, N. Vykhodtseva, S. Raymond, F. a Jolesz, K. Hynynen, MRI-guided targeted blood–brain barrier disruption with focused ultrasound: histological findings in rabbits, Ultrasound Med. Biol. 31 (2005) 1527–1537.
[23] J.J. Choi, M. Pernot, S.A. Small, E.E. Konofagou, Noninvasive, transcranial and localized opening of the blood–brain barrier using focused ultrasound in mice, Ultrasound Med. Biol. 33 (2007) 95–104.
[24] M. O'Reilly, A.C. Waspe, M. Ganguly, K. Hynynen, Focused-ultrasound disruption of the blood–brain barrier using closely-timed short pulses: influence of sonication parameters and injection rate, Ultrasound Med. Biol. 37 (2011) 587–594.
[25] N. McDannold, N. Vykhodtseva, F. a Jolesz, K. Hynynen, MRI investigation of the threshold for thermally induced blood–brain barrier disruption and brain tissue damage in the rabbit brain, Magn. Reson. Med. 51 (2004) 913–923.
[26] P.S. Tofts, G. Brix, D.L. Buckley, J.L. Evelhoch, E. Henderson, M.V. Knopp, et al., Estimating kinetic parameters from dynamic contrast-enhanced T1-weighted MRI of a diffusable tracer: standardized quantities and symbols, Magn. Reson. Imaging 232 (1999) 223–232.
[27] J. Park, Y. Zhang, N. Vykhodtseva, F. a Jolesz, N.J. McDannold, The kinetics of blood brain barrier permeability and targeted doxorubicin delivery into brain induced by focused ultrasound, J. Control. Release 162 (2012) 134–142.

[28] F. Vlachos, Y.-S. Tung, E.E. Konofagou, Permeability assessment of the focused ultrasound-induced blood–brain barrier opening using dynamic contrast-enhanced MRI, Phys. Med. Biol. 55 (2010) 5451–5466.
[29] F. Vlachos, Y.-S. Tung, E. Konofagou, Permeability dependence study of the focused ultrasound-induced blood–brain barrier opening at distinct pressures and microbubble diameters using DCE-MRI, Magn. Reson. Med. 830 (2011) 821–830.
[30] S.B. Raymond, J. Skoch, B.J. Bacskai, K. Hynyen, Modular design for *in vivo* optical imaging and ultrasound treatment in the murine brain, IEEE Trans. Ultrason. Ferroelectr. Freq. Control. 54 (2007) 431–434.
[31] S.B. Raymond, J. Skoch, K. Hynynen, B.J. Bacskai, Multiphoton imaging of ultrasound/Optison mediated cerebrovascular effects *in vivo*, J. Cereb. Blood Flow Metab. 27 (2007) 393–403.
[32] E.E. Cho, J. Drazic, M. Ganguly, B. Stefanovic, K. Hynynen, Two-photon fluorescence microscopy study of cerebrovascular dynamics in ultrasound-induced blood–brain barrier opening, J. Cereb. Blood Flow Metab. (2011) 1–11.
[33] T. Nhan, A. Burgess, K. Hynynen, Transducer design and characterization for dorsal based ultrasound exposure and two photon imaging of *in vivo* blood–brain barrier disruption in a rat model, IEEE Trans. Ultrason. Ferroelectr. Freq. Control. 60 (2013) 1376–1385.
[34] M.R. Dreher, W. Liu, C.R. Michelich, M.W. Dewhirst, F. Yuan, A. Chilkoti, Tumor vascular permeability, accumulation, and penetration of macromolecular drug carriers, J. Natl Cancer Inst. 98 (2006) 335–344.
[35] F. Yuan, M. Leunig, S.K. Huang, D.A. Berk, D. Papahadjopoulos, R.K. Jain, Microvascular permeability and interstitial penetration of sterically stabilized (stealth) liposomes in a human tumor xenograft, Cancer Res. (1994) 3352–3356.
[36] M.W. Dewhirst, S. Shan, Y. Cao, B. Moeller, F. Yuan, C.-Y. Li, Intravital fluorescence facilitates measurement of multiple physiologic functions and gene expression in tumors of live animals, Dis. Markers 18 (2002) 293–311.
[37] C.C. Michel, F.E. Curry, Microvascular permeability, Physiol. Rev. 79 (1999) 703–761.
[38] A.R. Pries, D. Neuhaus, P. Gaehtgens, Blood viscosity in tube flow: dependence on diameter and hematocrit, Am. J. Physiol. Heart Circ. Physiol. (1992) 1770–1778.
[39] B. Dehouck, L. Fenart, M.-P. Dehouck, A. Pierce, G. Torpier, R. Cecchelli, A new function for the LDL receptor: transcytosis of LDL across the blood–brain barrier, J. Cell Biol. 138 (1997) 877–889.
[40] R.L. Roberts, R.E. Fine, a Sandra, Receptor-mediated endocytosis of transferrin at the blood–brain barrier, J. Cell Sci. 104 (Pt 2) (1993) 521–532.
[41] A. Burgess, C.A. Ayala-Grosso, M. Ganguly, J.F. Jordão, I. Aubert, K. Hynynen, Targeted delivery of neural stem cells to the brain using MRI-guided focused ultrasound to disrupt the blood–brain barrier, PLoS One 6 (2011) e27877.
[42] R. Alkins, A. Burgess, M. Ganguly, G. Francia, R. Kerbel, W.S. Wels, et al., Focused ultrasound delivers targeted immune cells to metastatic brain tumors, Cancer Res. 73 (2013) 1892–1899.
[43] N. McDannold, N. Vykhodtseva, K. Hynynen, Blood–brain barrier disruption induced by focused ultrasound and circulating preformed microbubbles appears to be characterized by the mechanical index, Ultrasound Med. Biol. 34 (2008) 834–840.
[44] A. Burgess, E.E. Cho, L. Shaffaf, T. Nhan, C. Poon, K. Hynynen, The use of two-photon microscopy to study the biological effects of focused ultrasound on the brain, Proc. SPIE, 2012, pp. 822642–822647.
[45] C.X. Deng, F. Sieling, H. Pan, J. Cui, Ultrasound-induced cell membrane porosity, Ultrasound Med. Biol. 30 (2004) 519–526.
[46] N. Sheikov, N. McDannold, N. Vykhodtseva, F. Jolesz, K. Hynynen, Cellular mechanisms of the blood–brain barrier opening induced by ultrasound in presence of microbubbles, Ultrasound Med. Biol. 30 (2004) 979–989.